Climate
of the Past

Supplement of

Influence of temporally varying weatherability on CO₂-climate coupling and ecosystem change in the late Paleozoic

Jon D. Richey et al.

Correspondence to: Jon D. Richey (jdrichey@ucdavis.edu) and Isabel P. Montañez (ipmontanez@ucdavis.edu)

1   **Supplementary Materials and Methods**

2   **S1 Expanded Geologic and Paleogeographic Information**

3   The carbonate nodules from Montañez et al., (2007) utilized in this study were collected from well-developed and drained

4   paleosols from: 1) the Eastern Shelf of the Midland Basin (NC Texas), 2) Paradox Basin (SE Utah), 3) Pedregosa Basin (SC

5   New Mexico), 4) Anadarko Basin (SC Oklahoma), and 5) the Grand Canyon Embayment (NC Arizona) (Fig. 1a; Richey et

6   al., (2020)). The plant cuticle fossils come from localities in: 1) NC Texas (Lower Pease River [LPR], Lake Kemp Dam [LKD],

7   Parkey's Oil Patch [POP], and Mitchell Creek [MC]; all representing localities that also provided carbonate nodules or plant

8   organic matter [POM] for Montañez et al., (2007), 2) NC New Mexico (Kinney Brick Quarry [KB]), 3) SE Kansas (Hamilton

9   Quarry [HQ]), 4) SE Illinois (Lake Sara Limestone [LSL]), and 5) SW Indiana (sub-Minshall [SM]) (Fig. 1a, S2–4; Richey et

10   al., (2020)). These localities span a vast portion of the western equatorial portion of Euramerica during the Middle

11   Pennsylvanian through latest early Permian (Fig. 1b).

12

13   **S2 Biostratigraphic Correlations and Age Model**

14   NC Texas stratigraphy and the position of pedogenic carbonate samples from Montañez et al., (2007) and cuticle were

15   inferred from NC Texas conodont biostratigraphy and its relation to Permian global conodont biostratigraphy (Tabor and

16   Montañez, 2004; Wardlaw, 2005; Henderson, 2018). The specific correlations used are (C. Henderson, personal

17   communication, August 2019): (1) The Stockwether Limestone Member of the Pueblo Formation contains *Idiognathodus*

18   *isolatus*, indicating that the Carboniferous-Permian boundary (298.9 Ma) and base of the Asselian reside in the Stockwether

19   Limestone (Wardlaw, 2005). (2) The Gouldbusk Limestone Member of the Moran Formation contains a conodont that is likely

20   in the *I. whitei* zone. This conodont is also found in the Neva Limestone of Kansas and indicates a mid- to late Asselian age

21   (~295 Ma; Wardlaw, (2005)). (3) The Santa Anna Branch Shale and Coleman Junction Formations of the Cisco Gp contain

22   *Sweetognathus merrilli*, indicating that these two formations span the range of occurrence of *S. merrilli* of 297.2–298.9 Ma

23   (Wardlaw, 2005; Henderson, 2018). (4) The Hords Creek Limestone and Elm Creek Limestone Members of the Admiral and

24   Elm Creek Formations, respectively, contain *S.* (*Rabeignathus*) *bucaramangus*, indicating an age range of 294.2–293.5 Ma

25   (Wardlaw, 2005; Henderson, 2018). Specifically, the Elm Creek Limestone contains the top of the *S.* (*Rabeignathus*)

26   *bucaramangus* biozone indicating an age of 293.5 Ma and the likely position of the Asselian-Sakmarian boundary (C.

27   Henderson, Pers. Comm. 2019). (5) The Talpa Formation in the Albany Group contains abundant brachiopods and the fusulinid

28   taxon *Schwagerina crassitectoria*, indicating a likely Kungarian age.

29   Building upon this information, the plant and paleosol localities used in Montañez et al., (2007) were assigned ages using

30   these NC Texas biostratigraphic correlations, previous stratigraphic reconstructions (Tabor and Montañez, 2004; Montañez et

31   al., 2007), the ages for bracketing stages from the most recent geologic timescale (Ogg et al., 2016), and interpolating ages

32   between age-constraints using long-term sedimentation rates (Richey et al., 2020).

33   Age uncertainties for localities (Richey et al., 2020) account for both stratigraphic resolution and bracketing

34   geochronologic control, the latter a function of the age uncertainties for the latest Carboniferous and early Permian as reported

35   in the geologic timescales (Gradstein et al., 2012; Ogg et al., 2016). Chronostratigraphic assignments for the earliest Permian

36   deposits are extrapolated into the US midcontinent from a high-precision U-Pb calibrated succession in the Urals (Russia)

37   using the conodonts *S. merrilli* and *S. Bucaramangus* (298.9–293.8 Ma) and *S. crassitectoria* (293.4–290 Ma; Eros et al.,

38   (2012); Schmitz and Davydov, (2012)). Reported analytical uncertainties for the U-Pb ages were propagated from the

39   bracketing samples and used to assign temporal uncertainty to the pCO$_2$ curve (Richey et al., 2020). For the middle Permian

40   Clear Fork Group, age constraints and uncertainties are based on the Leonardian-Guadalupian Boundary (272.3 Ma) and

41   extrapolated from the closest high precision ages in the Capitanian (Gradstein et al., 2012; Ogg et al., 2016). The stratigraphic

42   uncertainties are assigned based on depositional setting: 1) ± 100 Kyr for the channel sandstones, 2) ± 1 Myr for restricted

43   shallow-water limestones, and 3) ± 4 Myr for paleosol-hosting, red mudstones and siltstones (Richey et al., 2020).

44

45   **S3 Paleosol Carbonate-Based pCO$_2$ Estimates**

46   **S3.1 Model**

47   pCO$_2$ estimates from Montañez et al., (2007) were generated using the carbonate CO$_2$ paleobarometer (Cerling, 1992):

48    $$CO_{2(atm)} = S_{(z)} \cdot \frac{\delta^{13}C_s - (1.0044 \cdot \delta^{13}C_r) - 4.4}{\delta^{13}C_a - \delta^{13}C_s}$$ (Eq. S1)

49   where $S_{(z)}$ is the concentration of soil-respired CO$_2$, $\delta^{13}C_S$ is the carbon isotopic composition of soil CO$_2$ (inferred from the

50    $\delta^{13}C$ of pedogenic calcite [$\delta^{13}C_{Calc}$]), $\delta^{13}C_r$ is the carbon isotopic composition of soil-respired CO$_2$ (inferred from the $\delta^{13}C$ of

time-equivalent organic matter [$\delta^{13}C_{OM}$]), and $\delta^{13}C_a$ is the carbon isotopic composition of atmospheric CO_2 (inferred from the $\delta^{13}C$ of time-equivalent marine carbonate [$\delta^{13}C_{Carb}$]).

In this study, we utilized a newer MATLAB model, the Paleosol Barometer Uncertainty Quantification model (PBUQ; Breecker, (2013)). PBUQ builds upon the original carbonate CO_2 paleobarometer (Eq. S1) by allowing the user to choose from all the most recently defined methods to calculate $S_{(z)}$, $\delta^{13}C_S$, $\delta^{13}C_r$, and MAT (used, along with the $\delta^{13}C_{Calc}$, to calculate $\delta^{13}C_a$ (Romanek et al., 1992)). PBUQ improves atmospheric CO_2 estimates by utilizing a Monte Carlo approach to fully propagate uncertainty in all input parameters, producing 10,000 CO_2 estimates from which the mean, median, and 16th and 84th percentile error estimates are generated (Breecker, 2013).

In the methods and this supplemental document, a full account is given of the input parameters used in the PBUQ model in this study and how those input parameters differ from Montañez et al., (2007). All other data and input parameters not presented here are unchanged from Montañez et al., (2007).

S3.2 $S_{(z)}$

Among paleosol barometer variables, $S_{(z)}$ represents the most significant uncertainty due to the lack of estimates of $S_{(z)}$ in modern soils (Montañez, 2013). $S_{(z)}$ was initially assigned values based on broad environmental interpretations (i.e., paleosols formed in deserts vs. temperate or tropical environments) or assigned a single constant value (5000 ppm) (Brook et al., 1983; Cerling, 1992). Montañez et al., (2007) improved upon these methods by inferring ranges of $S_{(z)}$ values via comparison of the morphology of fossil paleosols and modern analog soils. That approach subsequently improved further via analysis of $\delta^{13}C_{Carb}$ and $\delta^{13}C_{OM}$ in Holocene soils, defining a range of $S_{(z)}$ values for modern soils (Montañez, 2013). In this study, we utilize the latter option from Montañez (2013).

S3.3 $\delta^{13}C_r$ (Inferred from $\delta^{13}C_{OM}$)

Montañez et al., (2007) used the $\delta^{13}C$ of well-preserved plant fossil organic matter ($\delta^{13}C_{POM}$) from adjacent and roughly time-equivalent sediments as a proxy for $\delta^{13}C_r$. However, it is suggested that the use of plant organic matter can result in anomalously high pCO_2 estimates (Myers et al., 2012) and that the $\delta^{13}C$ of organic matter occluded within the targeted

76   carbonate nodules ($\delta^{13}C_{OOM}$) better estimates $\delta^{13}C_r$ (Myers et al., 2016), despite the possibility of post-deposition microbially-

77   mediated alteration (Wynn, 2007). Because of this, in this study, we utilize $\delta^{13}C_{OOM}$ as a proxy of $\delta^{13}C_r$ (Richey et al., 2020).

78   Carbonate nodules remaining from the analysis by Montañez et al., (2007) were powdered in a shatterbox and

79   approximately six grams of calcite were dissolved in 10% HCl. Decarbonated sediments where vacuum filtered on cellulose

80   nitrate filter paper. Approximately 250 mg of de-carbonated sediment was analyzed at the Stable Isotope Facility, University

81   of California, Davis. Notably, ~250 mg (the maximum amount that can be analyzed at the Stable Isotope Facility) was

82   necessary to produce the required 100 µg of carbon for isotopic analysis due to the low organic carbon content in pedogenic

83   carbonate nodules (range all samples ~.03–0.36% organic carbon).

84   A boxplot of $\delta^{13}C_{POM}$ vs. $\delta^{13}C_{OOM}$ shows that $\delta^{13}C_{OOM}$ is 3‰ more negative than $\delta^{13}C_{POM}$ with no overlap of error

85   envelops, indicating that $\delta^{13}C_{POM}$ and $\delta^{13}C_{OOM}$ are significantly different (Fig. S5). We attribute the difference in isotopes to

86   OOM samples that come directly from paleosol carbonate nodules, representing the same early glacial portion of a glacial

87   cycle, in contrast to plant organics, which are typically deposited in younger glacial mudstones. This indicates a temporal

88   separation of the two organic matter types of up to 10^4 yr.

89   Use of $\delta^{13}C_{OOM}$ increased pCO_2 estimates of ~30–100%, with the greatest change occurring at lower CO_2 levels. Notably,

90   the use of $\delta^{13}C_{OOM}$ resulted in fewer biologically untenable CO_2 estimates (i.e., two < 170 ppm, the level at which plants begin

91   to be severely affected by RuBisCo limitation due to CO_2 starvation (Ward et al., 2005; Gerhart and Ward, 2010) than the use

92   of $\delta^{13}C_{POM}$ (15 < 170 ppm). We take this result as further evidence for $\delta^{13}C_{OOM}$ being a more appropriate proxy for $\delta^{13}C_r$.

93

94   **S3.4 $\delta^{13}C_a$ (Inferred from $\delta^{13}C_{Carb}$)**

95   Montañez et al., (2007) calculated $\delta^{13}C_a$ from the $\delta^{13}C$ value of contemporaneous brachiopods (Grossman et al., 2008)

96   and the equation that describes the temperature-sensitive fractionation between marine calcite and atmospheric CO_2 (Romanek

97   et al., 1992):

98    $\varepsilon_{calcite-CO2} = 11.98(\pm0.13) - 0.12(\pm0.01) \cdot T(°C)$ (Eq. S2).

99   However, the shallow marine brachiopods used in Grossman et al., (2008) increase the possibility of post-depositional

100   alteration of the $\delta^{13}C$ signal. Instead, we utilize a recent compilation of deep-marine carbonate $\delta^{13}C$ (Naqing succession, Dian-

101 Qian-Gui Sea, China) because they show no evidence of sub-areal exposure, mitigating the possibility of post-depositional

102 alteration (Buggisch et al., 2011). These data and contemporaneous estimates of mean annual temperature (MAT; Tabor and

103 Montañez, (2005); Tabor et al., (2013)) were used in the Eq. S2 (Romanek et al., 1992) by PBUQ to estimate $\delta^{13}C_a$ (Richey et

104 al., 2020).

105 To accomplish this, the ages from Buggisch et al., (2011) were updated to reflect the most recent geologic timescale (Ogg

106 et al., 2016). Within the updated time series, if an individual $\delta^{13}C_{Carb}$ value occurred within ten Kyr of the age of an individual

107 paleosol, that value was used directly with an error of 0.2‰ (i.e., four times the error of $\delta^{13}C_{Carb}$ reported in Buggisch et al.,

108 (2011)). If such a value was not available, the two closest $\delta^{13}C_{Carb}$ values were averaged and used with an error of 0.4‰ to

109 account for the uncertainty in this method (Richey et al., 2020).

110 To check the validity of using the data from Buggisch et al., (2011), PBUQ was also run using a more recent $\delta^{13}C_{Carb}$

111 compilation (Chen et al., 2018), featuring data from both Grossman et al., (2008) and Buggisch et al., (2011). CO_2 estimates

112 from that model run did not significantly vary from runs using data from Buggisch et al., (2011), resulting in a change in CO_2

113 of 10s of ppm (range = ~1 to 80 ppm, with 85% of the data showing a change of <10 ppm). Due to this, we continued to use

114 data from Buggisch et al., (2011).

115

116 **S3.5 Changes to the PBUQ Model Code**

117 PBUQ model runs conducted in this study resulted in several biologically untenable CO_2 estimates for some localities

118 (i.e., ≤170 ppm; Gerhart and Ward, (2010)). To limit estimates below that threshold, two changes to the PBUQ Matlab code

119 were applied:

120 1) In the `soil_derived_component_of_soil_CO2` file,

```
121  for j = 1:m-1
122              if soilorder(j) == 1
123                  bestSz(j) = median(Mollisol_Sz);
124              elseif soilorder(j) == 2
125                  bestSz(j) = median(Alfisol_Sz);
126              elseif soilorder(j) == 3
127                  bestSz(j) = median(Aridisol_Sz);
128              elseif soilorder(j) == 4
129                  bestSz(j) = median(Vertisol_Sz);
130              elseif soilorder(j) == 5
```

```
131                    bestSz(j) = median(Andisol_Sz);
132                elseif soilorder(j) == 6
133                    bestSz(j) = median(Inceptisol_Sz);
134                end
```

(lines 460-473) were altered to

```
for j = 1:m-1
            if soilorder(j) == 1
                bestSz(j) = trimmean(Mollisol_Sz,25);
            elseif soilorder(j) == 2
                bestSz(j) = trimmean(Alfisol_Sz,25);
            elseif soilorder(j) == 3
                bestSz(j) = trimmean(Aridisol_Sz,25);
            elseif soilorder(j) == 4
                bestSz(j) = trimmean(Vertisol_Sz,25);
            elseif soilorder(j) == 5
                bestSz(j) = trimmean(Andisol_Sz,25);
            elseif soilorder(j) == 6
                bestSz(j) = trimmean(Inceptisol_Sz,25);
             end.
```

and

2) In the `monte_carlo_error_prop` file,

```
atm_CO2_estimate (1,:) = median(Ca)
```

(line 693) was altered to

```
atm_CO2_estimate (1,:) = trimmean(Ca, 25).
```

Code alteration one trimmed the means of the range of $S_{(z)}$ values used in the model by 25%. Likewise, code alteration two trimmed the ranges of values for each atmospheric CO_2 estimate by the model by 25%. A sensitivity analysis was performed using the following combinations: 1) trimmed $S_{(z)}$ means; untrimmed Monte Carlo estimates and 2) untrimmed $S_{(z)}$ means; trimmed Monte Carlo estimates. Ultimately, combination two was found to provide the least amount of estimates below the 170 ppm threshold and was utilized in this study.

S4 Stomatal-Based CO_2 Estimates

S4.1 Plant Fossil Localities

S4.1.1 Sub-Minshall

SM is a seasonally dry flora from sediments from the defunct Brazil Coal and Clay Company, Clay County, SW Indiana,

6

167 consisting almost exclusively of the dry-adapted plant species *Cordaites* and *Lesleya*, with rare wet-adapted elements and

168 abundant charcoal (DiMichele et al., 2016), though a separate wet-adapted Minshall flora also exists. In this study, we utilize

169 cuticles of the recently described species *C. minshallensis* (Šimůnek, (2018); Fig. S4a, Richey et al., (2020)).

170   The flora occurs in a shale stratum below the Minshall Coal and above the Upper Block Coal of the Brazil Formation.

171 The Upper Block Coal was included in the CO_2 compilation of Montañez et al., (2016) and is assigned a revised age of 313.09

172 Ma in this study (Richey et al., 2020). Due to this, we assign SM an age of 312.97 Ma. Furthermore, we assign an age

173 uncertainty of ± 0.2 Ma to represent the span of midcontinent major cyclothems (i.e., Long eccentricity, 0.4 My; Heckel,

174 (2013); Richey et al., (2020)).

175

176 **S4.1.2 Kinney Brick**

177   KB (Tinajas Member, Atrasado Formation, central New Mexico) is a *Konservat Lagerstätte* consisting of estuarine to

178 marine sediments preserving vertebrates, invertebrates, and plant fossils (Lucas et al., 2011). KB is a particularly important

179 plant fossil locality, preserving ~30 species, including lycopsids, sphenopsids, ferns, pteridosperms, coniferophytes,

180 taeniopterids, among others (DiMichele et al., 2013).

181   The age of KB is uncertain. Based on fossils preserved at KB, the locality was first assigned an early Permian age (Stukey,

182 1967). This assignment was revised to an early Virgilian age based on regional lithostratigraphy (Myers and McKay, 1976).

183 Later, the age was updated using its stratigraphic position and biostratigraphic indicators. The best estimate of age, drawn from

184 this evidence, is lower Missourian (middle Kasimovian) (Lucas et al., 2011). Of this evidence, the presence of the conodonts

185 *Idiognathodus corrugatus* and *I. cherryvalensis* is significant, as it allows correlation to the *I. confragu*s zone of the North

186 America Midcontinent region and, in turn, the Dennis cyclothem (Lucas et al., 2011; Heckel, 2013). Based on this information,

187 we assign KB an age of 305.7 Ma (i.e., corresponding to the interglacial portion of the Dennis cyclothem) and an age

188 uncertainty of ± 0.2 Ma to represent the span of midcontinent major cyclothems (Heckel, (2013); Richey et al., (2020)).

189   Typically, KB plants are carbonized and barren of cuticle, but a small collection of macrofossils at the University of

190 California Museum of Paleontology possesses degraded, but measurable cuticle. These cuticles were sampled, wet-mounted,

191 and observed under UV light. Though many degraded cuticles where sampled, including walchians, cordiataleans, and

peltisperms, this work produced a single viable cuticle species, identified as *Cordaites sp.* in DiMichele et al., (2013) (Fig. S4b; Richey et al., (2020)). However, recently, a new *Cordaites* species, *C. kinneyensis,* from KB was described (Šimůnek, 2018). Using the figures and description from Šimůnek, (2018), the cuticle utilized in this study was also found to be *C. kinneyensis* (Fig. S4b).

S4.1.3 Lake Sara Limestone

LSL is an informally named basal limestone of the Shumway Cyclothem, Mattoon Formation, McLeansboro Group, SE Illinois. LSL is found below the Shumway Limestone (part of the CO_2 reconstruction of Montañez et al., (2016) and given an updated age of 303.7 Ma in this study; Richey et al., (2020)) and above the Watson Coal, the next coal above the Calhoun Coal. The Calhoun Coal is also part of the CO_2 reconstruction of Montañez et al., (2016) and was given an updated age of ~304.13 Ma in this study (Richey et al., 2020). Given that they are part of two adjacent cyclothems, the Calhoun and Watson Coal is theoretically separated by ~400 Kyr (Heckel, 2013), giving the Watson Coal an age of 303.73 Ma. Due to this evidence, we assigned LSL an age of 303.71 Ma and again assigned an age uncertainty of ± 0.2 Ma (Richey et al., 2020).

Little information is available about the LSL flora as a whole, but in this study, we utilized measurements from the recently described species *Cordaites olneyensis* (Šimůnek, (2018); Fig. S4b; Richey et al., (2020)).

S4.1.4 Hamilton Quarry

HQ, southeastern Kansas, like KB, is a *Konservat Lagerstätte* consisting of paleochannel deposits that preserve vertebrates, invertebrates, and plant fossils (Cunningham, 1993). Conifers dominate the plant assemblage, in association with sphenopsids, ferns, pteridosperms, and rare lycopsids (Cunningham, 1993). This locality is particularly rich in formally described walchian conifers (Hernandez-Castillo et al., 2001; Hernandez-Castillo et al., 2003; Rothwell et al., 2005; Hernandez-Castillo et al., 2009a; Hernandez-Castillo et al., 2009c, b). In this study, we utilize previously prepared slides used in the formal descriptions of *Emporia royalii* (Hernandez-Castillo et al., 2009a), *E. lockardii* (Hernandez-Castillo et al., 2009c), and *E. cryptica* (Hernandez-Castillo et al., 2009b), reposited within the paleobotanical collections of the Kansas University Biodiversity Institute and Natural History Museum (Fig. S4d–f).

217   The age of HQ is problematic. Though the Hamilton paleochannel incised into cyclothemic sediments, inadequate

218   exposure and the lack of overlying beds precludes the assignment of an exact age (Salley et al., 2005). However, detailed

219   analysis and mapping of the surrounding area indicate that HQ is older than the Severy Shale but younger than the Hartford

220   Limestone Member of the Topeka Limestone (i.e., mid-Gzhelian [mid-Virgilian]; Salley et al., (2005)). This stratigraphic

221   evidence indicates that the most parsimonious stratigraphic position of HQ is within the Topeka cyclothem (Heckel, 2013).

222   Thus, we assign HQ an age of 302.7 Ma (i.e., the middle of the Topeka cyclothem) and an age uncertainty of $\pm$ 0.2 Ma (Richey

223   et al., 2020).

224

225   **S4.1.5 Parkey's Oil Patch, Lake Kemp Dam, Mitchell Creek**

226   These three localities are part of extensive plant fossil collections from the latest Pennsylvanian and through middle

227   Permian of NC Texas at the National Museum of Natural History (NMNH). Each represents channel-fill deposits from fluvial

228   to coastal plain settings. The assemblages of plants from these localities have not been formally described, but have been used

229   to reconstruct atmospheric CO_2 via paleosols (Montañez et al., 2007), track environmental change through time (DiMichele et

230   al., 2006), and investigate the radiation of peltasperms (DiMichele et al., 2005).

231   POP (uppermost Nacona Formation) cuticles were isolated from the ultimate shoots of walchian conifers and macerated.

232   *Walchia* sp. 2 was found to be suitable to measure stomatal number and geometry and is utilized in this study (Fig. S2a; Richey

233   et al., (2020)). LKD (basal Petrolia Formation) cuticle was isolated during exploratory palynological analysis by Carol Hotton

234   at the NMNH. After sorting and identification at UC Davis, the LKD cuticle assemblage was found to be monotypic, consisting

235   of a single walchian conifer morphotype, designated *Walchia* sp. 1 (Fig. S2b; Richey et al., (2020)). MC (upper Waggoner

236   Ranch Formation) cuticle was isolated via sieving of bulk sediment, producing a diverse assemblage of 14 cuticle morphotypes.

237   Of these, three morphotypes (a walchian conifer, voltzian conifer, and taeniopterid) produced enough cuticles to measure

238   stomatal parameters and are utilized in this study (Fig. S2c–e; Richey et al., (2020)). Note that the preliminary identification

239   of MC morphotypes is based on cuticle only and awaits confirmation via linking the cuticle types to macrofossils and

240   reproductive organs.

241   Because POP and MC are localities that also supplied paleosol carbonate for Montañez et al., (2007) and this study, and

242 because LKD is time equivalent to MC, the reformulated ages, and errors of the paleosols are used for these plant localities

243 (Richey et al., 2020).

244

245 **S4.1.6 Lower Pease River**

246   Collectively, the LPR (San Angelo and Blaine formations, Pease River Group) consists of eight plant fossil localities that

247 track a single plant-bearing stratum across Knox, King, and Stonewall counties in NC Texas (DiMichele et al., 2001). In this

248 study, we utilize material from two of these localities, Devil's Canyon and Buzzard Peak (Richey et al., 2020). LPR, like HQ,

249 POP, LKD, and MC, represents tidal paleochannel deposits from a coastal plain environment (DiMichele et al., 2001). The

250 LPR plant assemblage is diverse, consisting of members of the Equisetales, Coniferales, Ginkgoales, and Cycadales

251 (DiMichele et al., 2001). Using slides that were previously prepared by Cindy Looy in order to characterize the locality and

252 formally describe the extinct voltzian conifer *Lebowskia grandifolia* (Looy, 2007), we utilize *L. grandifolia* (Fig. S2f; Richey

253 et al., (2020)) and three addition morphotypes (two additional voltzian conifers and taeniopterid) in this study (Figs. S3a–c;

254 Richey et al., (2020)).

255   Since organic matter from Buzzard Peak was used and assigned an age in Montañez et al., (2007), we have updated

256 the age in the manner described above for the paleosols (Richey et al., 2020). Because LPR was placed in NC Texas

257 stratigraphy using the correlation of regional strata with global stratigraphy and the ages of the base of the Capitanian and the

258 Permian-Triassic Boundary, we used the combined error of those ages (0.5 My) as the age uncertainty of the LPR locality

259 (Richey et al., 2020).

260

261 **S4.2 Note on Walchian and Voltzian Conifers**

262   The earliest definitive conifers in the fossil record are the walchian conifers, or walchian Voltziales (*sensu* Rothwell et

263 al., (2005)), a paraphyletic group of small to large trees that were prominent members of late Pennsylvanian communities in

264 the drier areas of tropical Euramerican (Kerp et al., 1990; Rothwell et al., 1997). Walchians became ecologically important in

265 lowland floras in the Gzhelian and Asselian (Fig. 3c; Kerp, (2000); DiMichele et al., (2006)). They were diverse, represented

266 by several families and many genera. Walchian conifers had plagiotropic branches with helically arranged small linear to

267   narrow triangular leaves and stomata arranged in rows or bands ((Rothwell et al., 2005; Hernandez-Castillo et al., 2009c)). In

268   this study, we utilize walchian conifers from the HQ, POP, LKD, and MC floras (Fig. S2a–c, S4d–f).

269   The first definitive voltzian conifers, or voltzian Voltziales (*sensu* Rothwell et al., (2005)), are known from the Kungurian

270   of Texas (LPR Flora, Texas; Fig. S2f; DiMichele et al., (2001); Looy, (2007); Looy and Stevenson, (2014)) and northern Italy

271   (Forte et al., 2017) and possibly the Artinskian of Texas based on the tentative MC morphotype proposed in this study (Fig.

272   S2e). Earlier possible occurrences in the Asselian, and possibly as far back as the Sakmarian of New Mexico, await

273   confirmation from isolation of additional fossil material (Falcon-Lang et al., 2015; Falcon-Lang et al., 2016). The voltzian

274   conifers are distinctly different from the walchians in the characteristics of their foliage and ovuliferous cones (or fertile cones).

275   In contrast to walchians, the voltzians had irregular, orthotropic branching and quite variable, larger leaves which were

276   bifacially flattened and ovate to linear, with stomata scattered or organized within rows (Clement-Westerhof, 1987; Looy,

277   2007). In this study, we utilize voltzian conifers from the MC and LPR floras (Figs. S2e–f, S3a, c).

278

279   S4.3 Model

280   Recently, Franks et al., (2014) introduced a mechanistic stomatal model for estimating paleo-CO_2 as an alternative to

281   species-specific stomatal Index-based transfer functions. This mechanistic model uses anatomical and geochemical parameters

282   that are readily recovered from the plant fossils as proxies for variables in the classic photosynthesis model (Farquhar et al.,

283   1980). Stomatal size and number are used to calculate maximum stomatal conductance ($g_{c(max)}$) to CO_2, as well as operational

284   stomatal conductance ($g_{c(op)}$ [a fraction of $g_{c(max)}$]). These data are combined with leaf boundary layer and mesophyll

285   conductance to give total operational CO_2 conductance ($g_{c(tot)}$). Cuticle $\delta^{13}C$ values are used as a proxy for leaf $\delta^{13}C$ to estimate

286    $\frac{c_i}{c_a}$ (the ratio of internal CO_2 to atmospheric CO_2). These data are combined with the calculated assimilation rate (A_n) to calculate

287   atmospheric CO_2 via the following equation:

288    $$\text{Atmospheric } CO_2 = \frac{A_n}{g_{c(tot)} \cdot \left(1 - \frac{c_i}{c_a}\right)} \qquad\qquad\qquad \text{(Eq. S3)}$$

289   The mechanistic model has tested favorably against ice cores (Monnin et al., 2004), traditional stomatal estimates

290   (Kürschner et al., 1996; Richey et al., 2018), paleosol carbonate (Park and Royer, 2011)) and other proxies

291 (GEOCARBSULFvolc; Berner, (2008)). In addition, the mechanistic model is considered to be an improvement over

292 traditional stomatal proxy methods (i.e., Stomatal Index and Stomatal Density (SD; Woodward, (1987))) because the problems

293 of species specificity (due to the ability to accurately delineate plant fossils to the species level), unknown environmental

294 effects, and large error estimates at high CO_2 levels in the traditional methods.

295

296 **S4.4 Stomatal Methods and Model Parameters**

297 **S4.4.1 Measurements of Note**

298   Franks et al., (2014) states that if pore length (PL) can be measured directly from plant fossils, it should be used in place

299 of guard cell length (GCL), along with a PL to GCL scaler (s1) of 1 and an error (es1) of 0 (Richey et al., 2020). PL was used

300 for eight of the 15 morphotypes/species used in this study (Richey et al., 2020). For the remainder, no or very few stomatal

301 pores were preserved and, as a result, GCL was used (Richey et al., 2020). However, though there were not enough pores to

302 get a statistically significant measurement of PL for modeling, there were enough guard cells to calculate individual s1 values

303 for most morphotypes/species, which often vary significantly from the values suggested in Franks et al., (2014) (Richey et al.,

304 2020). In addition, for species/morphotypes were few guard cells exist, guard cell width (GCW) was estimated via GCL and

305 the suggested GCW (pair)/GCL scaler for gymnosperms and ferns (0.6; Tables S2; Richey et al., (2020)).

306   Note: Šimůnek, (2018) reported SD values of *Cordaites kinneyensis* as ~110-120/mm^2 for the abaxial surface and

307 ~70/mm^2 for the adaxial surface. Cuticles of *C. kinneyensis* measured in this study average ~65/mm^2. Using this information

308 and the descriptions in Šimůnek, (2018), it is likely that all cuticles isolated from University of California Museum of

309 Paleontology specimens are all adaxial. Because of this evidence, and the close match of SD for other species calculated here

310 and reported in Šimůnek, (2018), we have used the reported abaxial values of ~110-120/mm^2 from Šimůnek, (2018) in CO_2

311 modeling (Richey et al., 2020).

312

313 **S4.4.2 Plant $\delta^{13}C$**

314   The methods by which plant $\delta^{13}C$ ($\delta^{13}C_p$) was measured depended on the amount of cuticle available for analysis. For

315 LPR, cuticle was exceedingly abundant, such that it could be sorted into morphotypes to measure morphotype-specific $\delta^{13}C_p$

12

values (Richey et al., 2020). LKD, POP, KB, and LSL were monotypic cuticle assemblages and, therefore, cuticle was concentrated and morphotype-specific $\delta^{13}C_p$ values were generated (Richey et al., 2020). MC cuticles were less well preserved compared to other localities. As a result, most of the cuticle was mounted on slides to measure SD and stomatal geometry and the remainder was concentrated to produce a single locality-wide plant $\delta^{13}C$ value (Richey et al., 2020).

For SM, all available cuticle of *Cordaites minshallensis* was mounted for analysis by Šimůnek, (2018). Due to this, we used the average of the $\delta^{13}C_p$ of *Cordaites* species from KB (-24.2‰) and LSL (-25.2‰) as the $\delta^{13}C_p$ value of *C. minshallensis* (-24.8‰), with the standard deviation used as an error (i.e., 0.64‰, approximately three times the analytical error of analysis by the Stable Isotope Facility, University of California, Davis; Richey et al., (2020)).

For HQ, all material was previously mounted on slides for analysis by Hernandez-Castillo et al., (2009a, b, c). However, in 2016, bulk stratigraphic sediment samples were collected at HQ and subjected to exploratory biomarker $\delta^{13}C$ analysis in the laboratory of Michael Hren (University of Connecticut). Here, we use the average n-C_{27-31} *n*-alkane $\delta^{13}C$ calculated from all HQ stratigraphic samples as a substitute for cuticle $\delta^{13}C$. Studies have shown a range of isotopic offsets between compound-specific and bulk measurements (Conte et al., 2003; Diefendorf et al., 2011). In this study, we apply a 4‰ correction, the average measured fractionation of conifers (Diefendorf et al., 2015), to account for the fractionation during biosynthesis of *n*-alkanes. In addition, we use the standard deviation of all stratigraphic $\delta^{13}C$ values as the uncertainty (Richey et al., 2020).

For HQ biomarker analysis, bulk sediments were powdered in a shatterbox and freeze-dried for 24 hours. Approximately 300 g of sediment from each bulk stratigraphic sample was subjected to Soxhlet extraction in a 2:1 dichloromethane/methanol solution for 24 hours. *n*-alkanes were separated from the resulting total lipid extract via a combination of silica gel column chromatography and hexanes. Sulfur was removed from the resulting *n*-alkanes via activated copper chips. Finally, when necessary, the *n*-alkanes were further refined via urea adduction to remove contamination of branched and cyclic alkanes.

The carbon isotopic composition of n-alkanes was measured using a Thermo Scientific GC-Isolink connected to a Thermo Scientific MAT 253. Samples were injected into a split/splitless inlet at 300°C and separated on a 60 m x 20 mm x 0.25 µm DB-5 column with a He flow of 1.5 mL/min. GC oven temperature was increased from 60°C to 180°C at 12°C/min. At this temperature, the temperature was increased to 320°C at 4°C/min and held at 320°C for 10 minutes. Carbon isotopes are reported relative to VPDB and are analyzed relative to repeated measurements of an *n*-alkane isotope standard Mix A5 (Arndt

341   Schimmelman, Indiana University, Bloomington). Repeat analyses of this standard over a range of sample sizes yield a

342   standard deviation of 0.3‰.

343   Though the resulting $\delta^{13}C_p$ for HQ walchians (-24‰; Richey et al., (2020)) is more negative than the average $\delta^{13}C_p$ of

344   other walchian conifers measured directly (i.e., -22.75 ± 0.91‰ from POP and LKD walchians), the assigned uncertainty

345   (±1.6‰) is large enough to account for the uncertainty in both the method used to estimate $\delta^{13}C_p$ and the reported fractionation

346   of modern conifers (Diefendorf et al., 2015).

347

348   **S4.4.3 Note on $\delta^{13}C_p$**

349   Recently, Porter et al., (2017) suggested a correction should be applied to $\delta^{13}C_p$ values used in models such as PBUQ

350   (Breecker, 2013) and the mechanistic stomatal CO_2 model (Franks et al., 2014), especially when $\delta^{13}C_p$ is used to predict $\delta^{13}C_a$,

351   due to the influence of phylogeny and atmospheric $O_2:CO_2$ ratio. However, in this study, $\delta^{13}C_a$ was independently calculated

352   from deep-marine $\delta^{13}C_{Carb}$ (Buggisch et al., 2011) and Eq. S2 (Romanek et al., 1992)), possibly negating the need for such a

353   correction. Furthermore, we calculated $\delta^{13}C_p$ values ranging from -22.1‰ to -25.2‰ (mean -24.04‰) and $\delta^{13}C_{POM}$ and

354     $\delta^{13}C_{OOM}$ values ranging from -20.5‰ to -27.2 (mean -23.37‰). Using the independently inferred $\delta^{13}C_a$ values, we calculate a

355   mean observed fractionation between $\delta^{13}C_a$ and $\delta^{13}C_p$, $\delta^{13}C_{POM}$, and $\delta^{13}C_{OOM}$ of -18.62‰, within the range of observed

356   fractionation reported for modern gymnosperms (Arens et al., 2000; Diefendorf et al., 2010).

357   Nevertheless, to assess the effect, the correction for gymnosperms (-2.95‰; Porter et al., (2017)) was applied to $\delta^{13}C_p$

358   and the mechanistic stomatal model was rerun with those values, resulting in CO_2 increased 50–100% over those without the

359   correction, such that values that fit comfortably within the range paleosol-based estimates (Figs. 2a, S1a) were elevated relative

360   to the paleosol-based estimates. We interpret those results and the close match of the observed fractionation to fractionation in

361   modern gymnosperms as indicating that the correction is not needed in the context of this study.

362

363   **S5 Late Pennsylvanian and Early Permian pCO₂ Compilation and Analysis**

364   In this study, we present a compilation of late Pennsylvanian and early Permian pCO₂ estimates by combining estimates

365   from this study with those of Montañez et al., (2016) (Richey et al., 2020). The carbonate nodules, rhizolith samples, and

14

pteridosperm leaves used in Montañez et al., (2016) are from cyclothemic sediments from the Illinois Basin, USA, with addition paleosols coming from the Appalachian Basin, USA and the Donets Basin, Ukraine. Ages for localities used in Montañez et al., (2016) were revised and assigned uncertainties based on the stratigraphic relationship of each locality to one another and the proximity to well-dated intervals (e.g., stage boundaries; correlation to U-Pb calibrated cyclothems in the Donets Basin; Eros et al., (2012)) to reflect changes made to overlapping localities from Montañez et al. (2007) (Richey et al., 2020). Specifically, the ages from Montañez et al. (2016) were assigned uncertainties according to the following criteria: 1) localities that were closest stratigraphically to well-known and -constrained stage boundaries were assigned an error of 50 kyrs, 2) localities that occur within a 400-kyr Midcontinent cyclothem were assigned an error of 100 kyrs, 3) localities that fall within Midcontinent cyclothems whose ages are uncertain were assigned an error of 500 kyrs, and 4) localities from the Donets Basin were assigned an error of 100 kyrs (Richey et al., 2020).

Note: a few CO_2 estimates from Montañez et al. (2016) were revised during this study (Richey et al., 2020). These revised estimates do not affect the trends or interpretations presented in Montañez et al. (2016).

S6 Truncation of Age Uncertainties

The CO_2 and O_2:CO_2 age uncertainties were truncated for the LOESS analysis, constrained by the relative stratigraphic position of individual paleosols and plant fossil localities (Richey et al., 2020). Age uncertainties for adjacent localities cannot overlap because they are individual stratigraphic units separated by sediments, and, therefore, they cannot be the same age. Because of this, the individual age uncertainties were trimmed such that the errors for two adjacent samples are separated by at least 2000 years. The 2000-year separation threshold was applied because the long-term sediment accumulation rate for NC Texas sediments is 2–10cm/1000 yrs and each locality in the dataset is separated by at least 20 cm of sediment (minimum separation is 3 m).
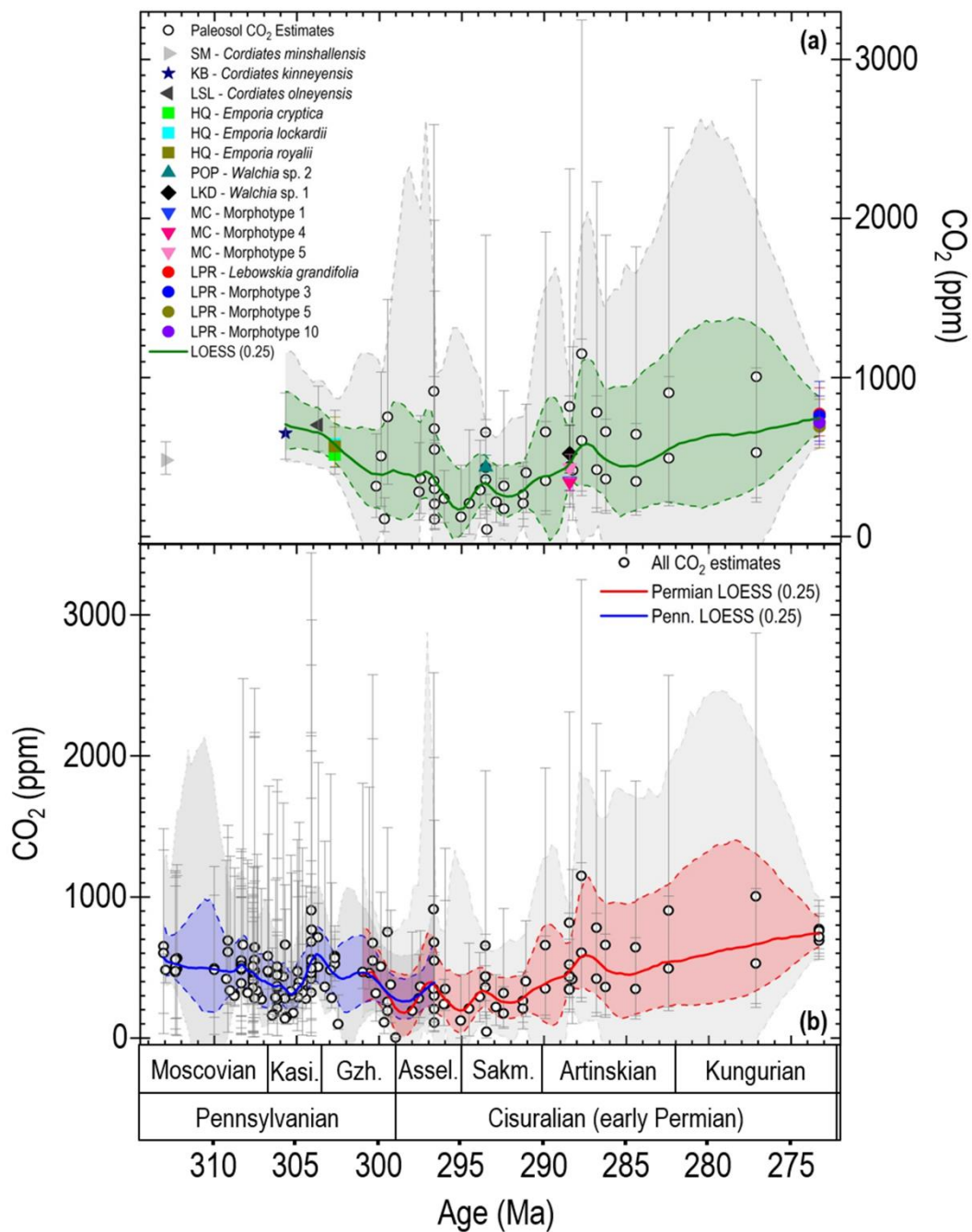
Supplemental Figures

15

389

Figure S1: Comparison of the confidence intervals of LOESS analyses of this study and the Late Pennsylvanian and early Permian pCO₂ compilation and presentation of the error of individual pCO₂ estimates. (a) pCO₂ estimates from this study and LOESS analysis. Plants from SM (*Cordaites minshallensis*), KB (*C. kinneyensis*), LSL (*C. olneyensis*), HQ

16

393   (*Emporia cryptica*, *E. lockardii*, *E. royalii*,), and LPR (*Lebowskia grandifolia*) that provided stomatal-based estimates are

394   formally described (Looy, 2007; Hernandez-Castillo et al., 2009a; Hernandez-Castillo et al., 2009c, b; Šimůnek, 2018). Plants

395   from POP (*Walchia* sp. 2), LKD (*Walchia* sp. 1), MC (morphotype 1, morph. 4, morph. 7,), LPR (morph. 3, morph. 5, morph.

396   10) are preliminarily described in this study. CO_2 error bars indicate the 16th and 84th percentiles. The gray shading is the 95%

397   confidence interval (CI); the green shading in the 75% CI. **(b)** $p$$CO_2$ compilation (this study and Montañez et al., (2016); open

398   circles) and LOESS analysis. The light and dark gray shading are the 95% CI; the red and blue shading in the 75% CI. Data

399   was divided into separate Pennsylvanian and Permian curves, with significant overlap around the Pennsylvanian-Permian
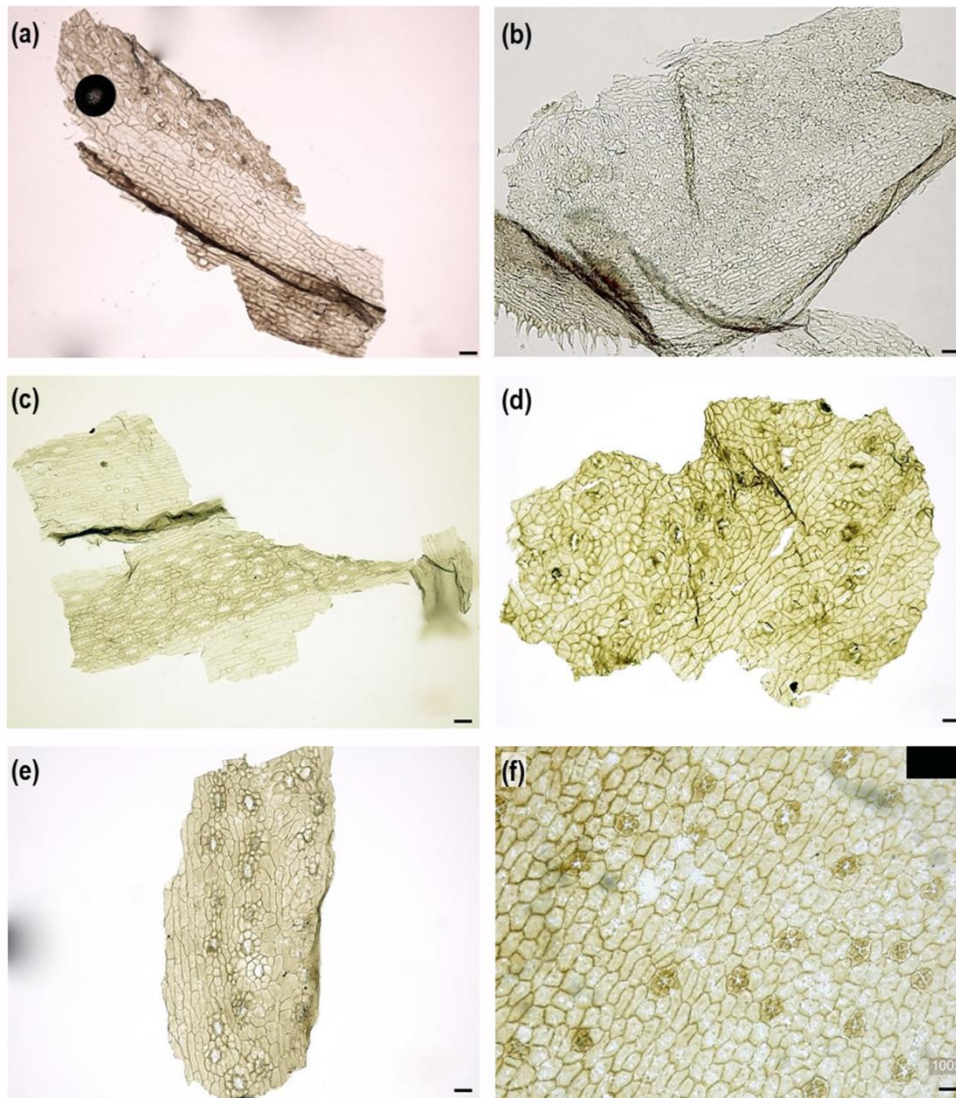
400   Boundary.

17

401

Figure S2: Permian cuticle morphotypes and species used to generate stomatal-based pCO$_2$ estimates. (a) *Walchia* sp.
#2, POP, Smithsonian National Museum of Natural History (NMNH) specimen #USNM-528666-Wsp2-CS11-cuticle2. **(b)**
Walchia sp. #1, LKD, NMNH specimen #USNM-40629-C. **(c)** Morphotype 4, MC, tentatively identified as a taeniopterid,
NMNH specimen #USNM-32138-MC-CS25-cuticle1. **(d)** Morphotype 5, MC, tentatively identified as a voltzian conifer,
NMNH specimen #USNM-32138-MC-CS5-cuticle2. **(e)** *Lebowskia grandifolia*, LPR (Looy, 2007), University of California
Museum of Paleontology specimen #BP-42104-CS67-SSL1. **(f)** Morphotype 1, MC, tentatively identified as a walchian
conifer, NMNH specimen #USNM-32138-MC-CS11-cuticle8 Scale for (a)–(f) 49.2 µm

18

409
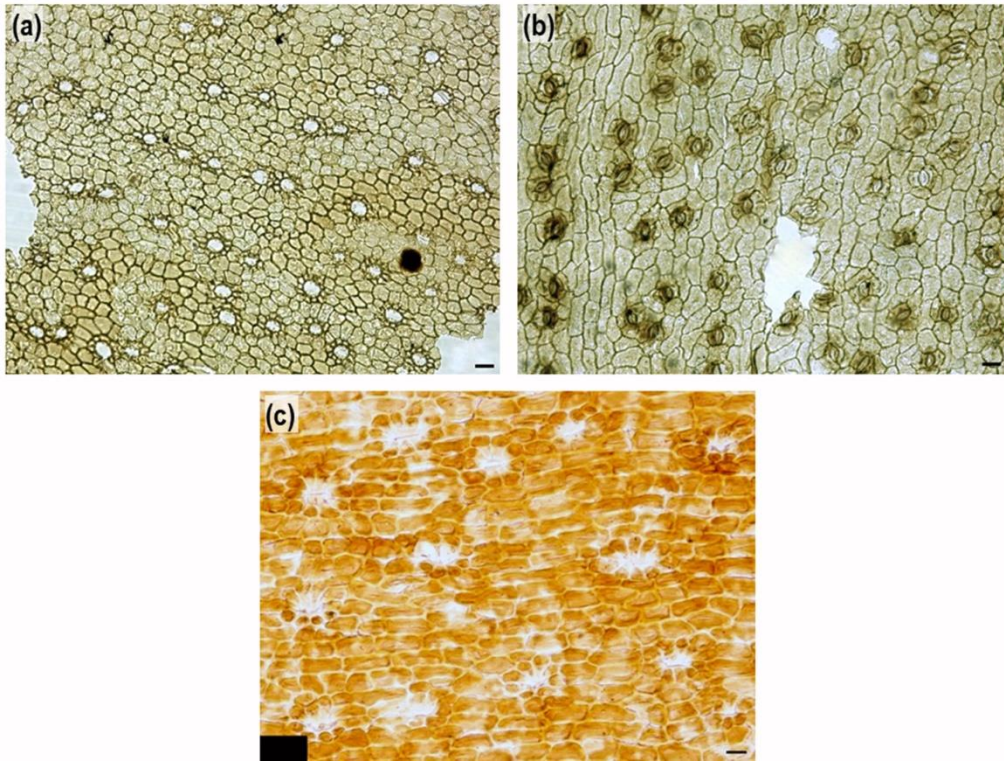
Figure S3: Additional Permian cuticle morphotypes used to generate stomatal-based pCO$_2$ estimates. (a) Morphotype
5, LPR, identified as a voltzian conifer, University of California Museum of Paleontology (UCMP) specimen #BP-42104-
CS38. **(b)** Morphotype 10, LPR, identified as a taeniopterid, UCMP specimen #BP-42104-CS32. Scale for (a) and (b) 49.2
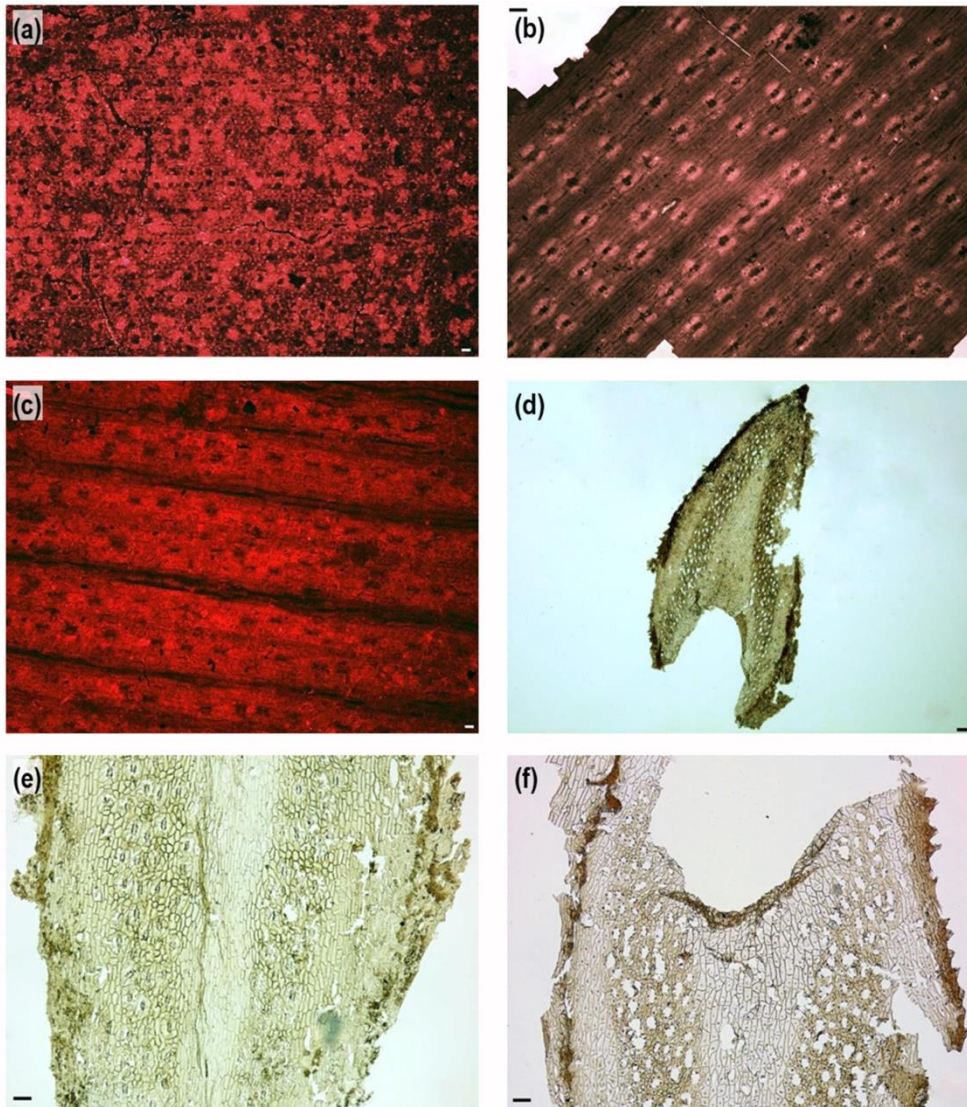µm. **(c)** Morphotype 3, LPR, identified as a voltzian conifer, UCMP specimen #BP-42104-CS68-SSL2. Scale 20 µm.

19

414

Figure S4: Pennsylvanian species used to generate stomatal-based pCO$_2$ estimates. **(a)** *Cordaites minshallensis*, SM (Šimůnek, 2018), Smithsonian National Museum of Natural History (NMNH) specimen #USNM-38878-RSB002A. Scale 24.6 µm. **(b)** *C. kinneyensis*, KB (DiMichele et al., 2013; Šimůnek, 2018), University of California Museum of Paleontology specimen #PA1337-UCMP200107-cuticle1. Scale 49.2 µm. **(c)** *C. olneyensis*, LSL (Šimůnek, 2018), NMNH specimen #USNM-38882-Slide6-cuticle5. Scale 24.6 µm. **(d)** *Emporia cryptica*, HQ (Hernandez-Castillo et al., 2009b), Kansas University Natural History Museum (KUNHM) specimen #KU28170. Scale 125 µm. **(e)** *E. lockardii*, HQ, KUNHM specimen #KU27968. Fig. 5a,c in Hernandez-Castillo et al., (2009c). Scale 49.2 µm. **(f)** *E. royalii*, HQ, KUNHM specimen #KU28553.

20

422   Fig. 5b, d in Hernandez-Castillo et al., (2009a). Scale 49.2 µm
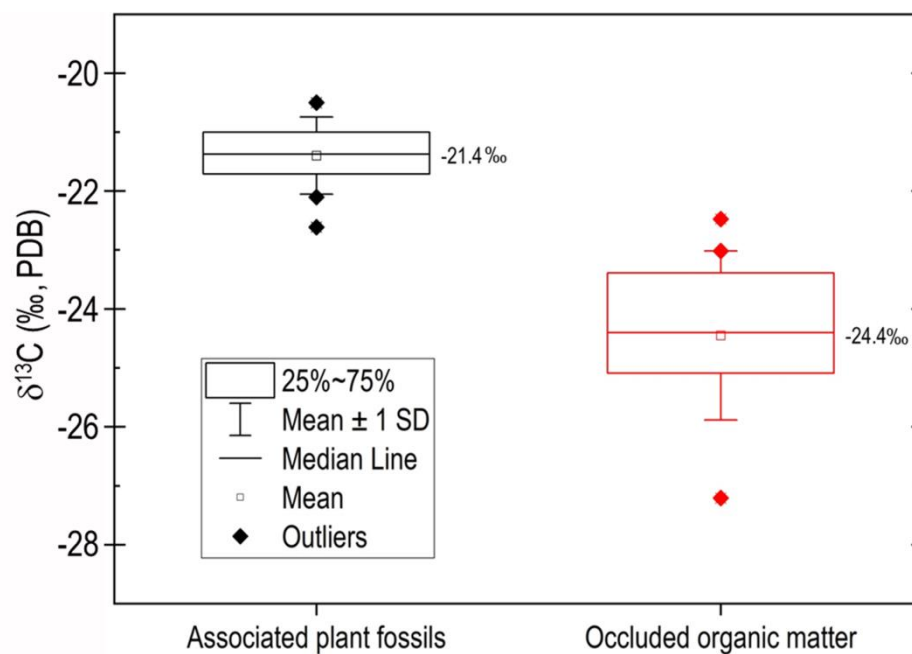
423

424

425

426

427

428

429

430

431

432

433

434

435

436

437

Figure S5: Box and whisker plot of $\delta^{13}C_{OM}$ used in PBUQ (Breecker, 2013) modeling by type.

439

308 Ma   290 Ma

▼ Global CO2 consumption rate   ▬ ▬ ▬ Linear regression fit of model outputs   ▬▬▬ Steady-state silicate weathering flux
✚ Steady-state atmospheric CO₂ for each time slice
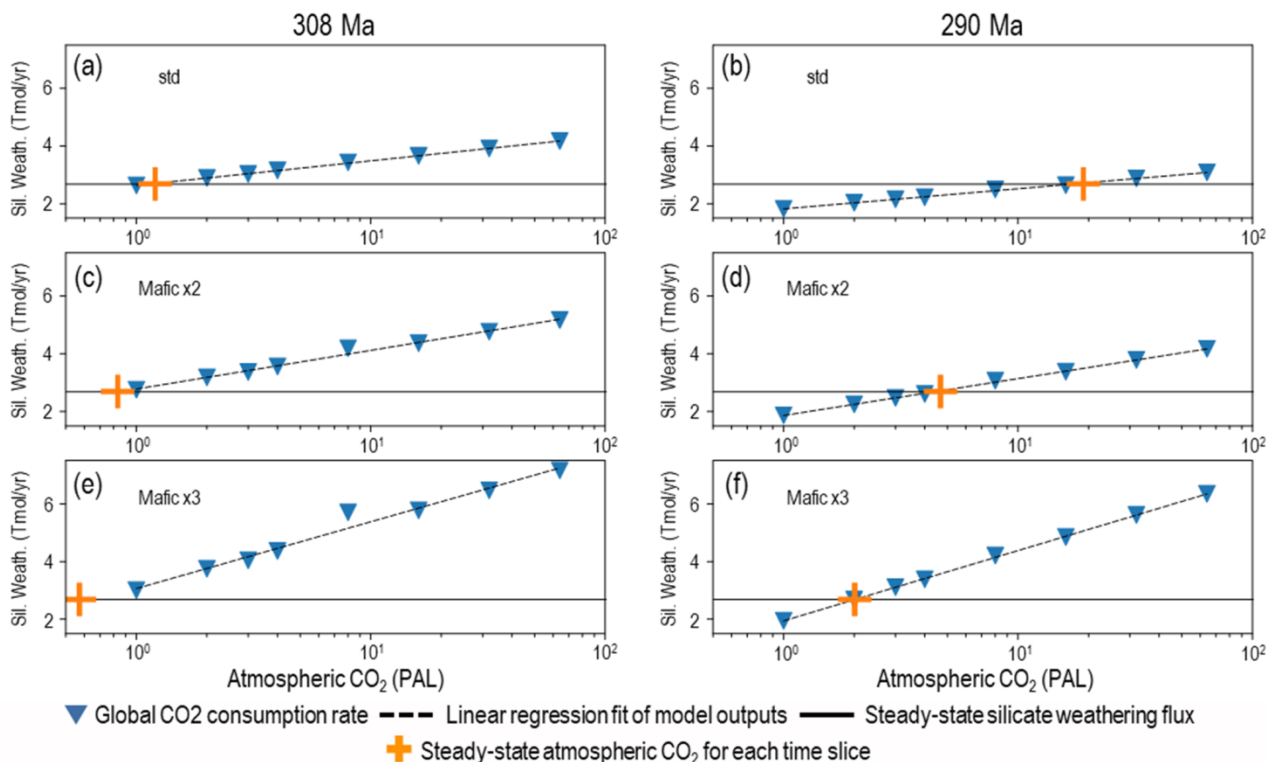
440

441   **Figure S6: Modeled global consumption rate of CO₂ through silicate weathering as a function of a range of initial**

442   **atmospheric CO₂ concentrations and varying surface area of outcropping mafic rock available for weathering**

443   **generated using the GEOCLIM model**. Global silicate weathering flux (y-axis) is calibrated to present-day global flux of

444   2.5×10^{12} moles of CO_2 consumed by silicate weathering (Gaillardet et al., 1999; Goddéris et al., 2017). Global CO_2

445   consumption rate (Tmoles/yr) through silicate weathering is modeled for eight initial atmospheric CO_2 concentrations

446   (logarithmic-scale relative to PAL (280 ppm)) and levels of weatherability based on simulated paleotopographic and climate

447   conditions at 308 Ma (left panels) and 290 Ma (right panels). The 'steady-state silicate weathering flux' is the level needed to

448   balance the level of solid Earth CO_2 degassing and to maintain steady-state atmospheric CO_2 above the threshold for continental

449   ice sheet initiation before the uplift of the Hercynian orogen (350 Ma; 1120 ppm (Lowry et al., 2014)). The level of solid Earth

450   CO_2 degassing, assumed to be constant between 350 to 290 Ma, is calibrated to the present-day global flux of CO_2 consumed

451   by silicate weathering and predicates that the CO_2 sink exactly balances the CO_2 source (cf. Zeebe and Caldeira, (2008)). The

452   intercept of the linear regression fit and the steady-state silicate weathering flux denotes the steady-state atmospheric CO_2

23

453 concentration for each time slice. **(a–b)** Reference simulation using surface area of outcropping mafic rock ('std') for the late

454 Carboniferous of Godderis et al., (2017). Results of sensitivity experiments are shown for a doubling **(c–d)** and tripling **(e–f)**

455 of the surface area of outcropping mafic rocks. At 308 Ma (Middle Pennsylvanian and peak uplift of CPM), the steady-state

456 atmospheric CO_2 concentration progressively shifts towards lower values staying well below the glacial threshold (840 ppm;

457 Lowry et al., (2014)) regardless of surface area of outcropping mafic rock. A substantially higher steady-state atmospheric

458 CO_2 concentration (3500 ppm), well above the glacial threshold for this time (560 ppm; Lowry et al., (2014)) is predicted for

459 the reference simulation ('std'; (d)). Increasing the surface area of outcropping mafic rocks strongly impacts CO_2 concentration,

460 which decreases to ~650 ppm for a doubling of exposed mafic rocks (e) and ~350 ppm for a tripling (f).

461

462 **Supplementary Table**

463

Table S1: Description of mechanistic model parameters		
Input	**Description**	**Method/Approximation/References**
D_{ab}	Stomatal density (m^2) on abaxial surface (average over stomatal and non-stomatal areas).	Franks et al., (2014) specifies the use of leaf-wide stomatal density (SD). Due to this, most SD measurements were made at 100x to ensure that the largest area possible was measured and leaf-wide SD was approximated.
eD_{ab}	Error in D_{ab} (m^2).	Standard Error of the Mean (SEM) of approximated leaf-wide stomatal density.
D_{ad}	Stomatal density (m^2) on adaxial surface (average over stomatal and non-stomatal areas).	Approximated Leaf-wide SD values used varied depending on whether individual morphotype was hypostomatic or amphistomatic.
eD_{ad}	Error in D_{ad} (m^2).	SEM of leaf-wide stomatal density. Values used varied depending on whether individual morphotype was hypostomatic or amphistomatic.
GCL_{ab}	Guard cell length (m) on the abaxial surface.	Franks et al., (2014) calls for Guard Cell Length (GCL) (and a scaling factor to estimate Pore Length [PL] from GCL; PL/GCL, designated parameter s1) to be used as a model parameter, but notes that Pore Length (PL) should be used if possible (with s1 = 0). The method used for each morphotype depended on the preservation of guard cells and pores. See Supplemental Materials and Methods text for details.
$eGCL_{ab}$	Error in GCL_{ab} (m).	SEM of PL or GCL (m).
GCL_{ad}	Guard cell length (m) on the adaxial surface.	PL or GCL value used varied depending on whether individual morphotype was hypostomatic or amphistomatic.
$eGCL_{ad}$	Error in GCL_{ad} (m).	SEM of PL or GCL (m). Values used varied depending on whether individual morphotype was hypostomatic or amphistomatic.
GCW_{ab}	Single guard cell width	Franks et al., (2014) calls for Guard Cell Width (GCW) to be used directly, if

	(m) on the abaxial surface.	possible. If not, Franks et al., (2014) suggests using GCL and a suggested GCW (pair)/GCL scaler for gymnosperms and ferns. The method used for each morphotype depended on the preservation of guard cells. See Supplemental Materials and Methods text for details.
eGCW$_{ab}$	Error in GCW$_{ab}$ (m).	SEM of GCW or two times the GCW error if scaled from GCL. See Supplemental Materials and Methods text for details.
GCW$_{ad}$	Single guard cell width (m) on the adaxial surface.	GCW or scaled GCL values used varied depending on whether individual morphotype was hypostomatic or amphistomatic.
eGCW$_{ad}$	Error in GCW$_{ad}$ (m).	SEM of GCW or two times the GCW error if scaled from GCL values used varied depending on whether individual morphotype was hypostomatic or amphistomatic.
$\delta^{13}C_p$	The ratio of $^{13}C/^{12}C$ isotopes in leaf material (PDB; ‰).	Most cuticle $\delta^{13}C$ was analyzed at the Stable Isotope Facility, University of California, Davis. For Hamilton Quarry (HQ), *n*-alkane average n-C$_{27-31}$ $\delta^{13}C$ was measured in the laboratory of Dr. Michael Hren at the University of Connecticut. For SM plants, the average $\delta^{13}C$ of other *Cordaites* species was used as insufficient material was available for analysis. See Supplemental Materials and Methods text for details.
e$\delta^{13}C_p$	Error in $\delta^{13}C_p$ (PDB; ‰).	Used UC Davis Stable Isotope Facility analytical precision of ±0.2‰ for most samples. For HQ, we used the standard deviation of the stratigraphic samples collected in 2016. For SM plants, we used the standard deviation of the $\delta^{13}C$ of other *Cordaites* species. See Supplemental Materials and Methods text for details.
$\delta^{13}C_a$	The ratio of $^{13}C/^{12}C$ isotopes in (paleo-) atmosphere air, relative to that in the PDB standard (‰).	We utilize the equation that describes the temperature-dependent enrichment of $\delta^{13}C$ in biogenic calcite (Romanek et al., 1992) and $\delta^{13}C$ values deep-marine carbonates (Buggisch et al., 2011) and contemporaneous estimates of mean annual temperature (Tabor and Montañez, 2005; Tabor et al., 2013; Montañez et al., 2016).
e$\delta^{13}C_a$	Error in $\delta^{13}C_a$.	Used suggested error of 1‰.
CO$_0$	Atmospheric CO_2 concentration associated with A$_0$ (ppm) (e.g., present-day value).	Used the present CO_2 level of 400 ppm.
A$_0$	The photosynthetic rate at CO$_0$ (μmol/m^2/s).	Franks et al., (2014) suggests the value of 10 μmol/m^2/s for conifers and based on published measurements from extant plants. For the two taeniopterid morphotypes, we use value reported suggested for ferns and cycads (6 μmol/m^2/s).
eA$_0$	Error in A$_0$.	Used the suggested error of 1 μmol/m^2/s.
g$_b$	Boundary layer conductance to CO_2 (mol/m^2/s).	Used the suggested value of 2 mol/m^2/s.
eg$_b$	Error in g$_b$.	Used the suggested error of 0.1 mol/m^2/s.
s1	Scaling from guard cell length (GCL) to stomatal pore length (Pl).	The values used varied depending PL or GCL length was used. When PL was used directly, we used 0 as the scaler is not needed. When GCL was utilized, the value of the suggested s1 for gymnosperms and ferns (0.33) or an empirically derived s1 from stomatal measurements was used.
es1	Error in s1.	The values used varied depending PL or GCL length was used. When PL was directly used, we used 0 as the scaler is not needed. When GCL was utilized, the

		value of the suggested es1 (0.05) was used.
s2	Scaling from single guard cell width (GCW) to stomatal depth (l).	Used the suggested value of 1.
es2	Error in s2.	Used the suggested error of 0.05.
s3	Scaling from the area of a circle with the diameter of pore length to a_{max} (maximum area of the stomatal pore).	Used the suggested value for gymnosperms and ferns of 0.5.
es3	Error in s2.	Used the suggested error of 0.025.
s4	Scaling from maximum conductance to CO_2 ($g_{c(max)}$) to operational conductance to CO_2 ($g_{c(op)}$).	Used the suggested value of 0.2.
es4	Error in s4.	Used the suggested error of 0.02.
s5	Scaling from photosynthetic rate (A) to mesophyll conductance to CO_2 (g_m).	Used the suggested generic value of 0.013.
es5	Error in s5.	Used the suggested error of 0.00065.

464

465 **Table S1: Description of mechanistic model parameters as defined in Franks et al., (2014) and the methods used in this**

466 **study to measure or infer values.** See Richey et al., (2020) for specific values used in the mechanistic model.

467

468 **References**

469 Arens, N. C., Jahren, A. H., and Amundson, R.: Can C^3 plants faithfully record the carbon isotopic composition of atmospheric

470 carbon dioxide?, Paleobiology, 26, 137–164, https://doi.org/10.1666/0094-8373(2000)026<0137:CCPFRT>2.0.CO;2, 2000.

471 Berner, R. A.: Addendum to "Inclusion of the Weathering of Volcanic Rocks in the GEOCARBSULF Model": (R. A. Berner,

472 2006, V. 306, p. 295–302), Am. J. Sci., 308, 100–103, https://doi.org/10.2475/01.2008.04, 2008.

473 Breecker, D. O.: Quantifying and understanding the uncertainty of atmospheric CO_2 concentrations determined from calcic

474 paleosols, Geochem. Geophys. Geosy., 14, 3210–3220, https://doi.org/10.1002/ggge.20189, 2013.

475 Brook, G. A., Folkoff, M. E., and Box, E. O.: A world model of soil carbon dioxide, Earth Surf. Proc. Land., 8, 79–88,

476 https://doi.org/10.1002/esp.3290080108, 1983.

477 Buggisch, W., Wang, X., Alekseev, A. S., and Joachimski, M. M.: Carboniferous–Permian carbon isotope stratigraphy of

478 successions from China (Yangtze platform), USA (Kansas) and Russia (Moscow Basin and Urals), Palaeogeogr. Palaeocl.,

479 301, 18–38, https://doi.org/10.1016/j.palaeo.2010.12.015, 2011.

480 Cerling, T. E.: Use of carbon isotopes in paleosols as an indicator of the pCO$_2$ of the paleoatmosphere, Global Biogeochem.

481 Cy., 6, 307–314, https://doi.org/10.1029/92GB01102, 1992.

482 Chen, J., Montañez, I. P., Qi, Y., Shen, S., and Wang, X.: Strontium and carbon isotopic evidence for decoupling of pCO$_2$

483 from continental weathering at the apex of the late Paleozoic glaciation, Geology, 46, 395–398,

484 https://doi.org/10.1130/G40093.1, 2018.

485 Clement-Westerhof, J. A.: Aspects of Permian palaeobotany and palynology, VII. the majonicaceae, a new family of late

486 Permian conifers, Rev. Palaeobot. Palyno., 52, 375–402, https://doi.org/10.1016/0034-6667(87)90066-2, 1987.

487 Conte, M. H., Weber, J. C., Carlson, P. J., and Flanagan, L. B.: Molecular and carbon isotopic composition of leaf wax in

488 vegetation and aerosols in a northern prairie ecosystem, Oecologia, 135, 67–77, https://doi.org/10.1007/s00442-002-1157-4,

489 2003.

490 Cunningham, C. R.: Hamilton Fossil-Lagerstätte (Upper Pennsylvanian, Greenwood County, Kansas): Internal Stratigraphy

491 and Addition to the Microfossil Assemblage, Trans. K.S. Acad. Sci., 96, 131–139, https://doi.org/10.2307/3628324, 1993.

492 Diefendorf, A. F., Mueller, K. E., Wing, S. L., Koch, P. L., and Freeman, K. H.: Global patterns in leaf ^{13}C discrimination and

493 implications for studies of past and future climate, Proc. Natl. Acad. Sci. U.S.A., 107, 5738–5743,

494 https://doi.org/10.1073/pnas.0910513107, 2010.

495 Diefendorf, A. F., Freeman, K. H., Wing, S. L., and Graham, H. V.: Production of n-alkyl lipids in living plants and

496 implications for the geologic past, Geochim. Cosmochim. Acta, 75, 7472–7485, https://doi.org/10.1016/j.gca.2011.09.028,

497 2011.

498 Diefendorf, A. F., Leslie, A. B., and Wing, S. L.: Leaf wax composition and carbon isotopes vary among major conifer groups,

499 Geochim. Cosmochim. Acta, 170, 145–156, https://doi.org/10.1016/j.gca.2015.08.018, 2015.

500 DiMichele, W. A., Mamay, S. H., Chaney, D. S., Hook, R. W., and Nelson, W. J.: An Early Permian flora with Late Permian

501 and Mesozoic affinities from north-central Texas, J. Paleontol., 75, 449–460, https://doi.org/10.1666/0022-

502   3360(2001)075<0449:AEPFWL>2.0.CO;2, 2001.

503   DiMichele, W. A., Kerp, H., Krings, M., and Chaney, D. S.: The Permian peltasperm radiation: evidence from the southwestern

504   United States, in: The Nonmarine Permian, edited by: Lucas, S. G., and Zeigler, K. E., New Mexico Museum of Natural

505   History and Science Bulletin, New Mexico Museum of Natural History and Science, Albuquerque, NM, 67–79, 2005.

506   DiMichele, W. A., Tabor, N. J., Chaney, D. S., and Nelson, W. J.: From wetlands to wet spots: environmental tracking and the

507   fate of Carboniferous elements in Early Permian tropical floras, in: Wetlands through time, edited by: Greb, S. F., and

508   DiMichele, W. A., Geological Society of America Special Papers, The Geological Society of America, Boulder, CO, 223–

509   248, 2006.

510   DiMichele, W. A., Wagner, R. H., Bashforth, A. R., and Álvárez-Vazquez, C.: An update on the flora of the Kinney Quarry

511   of central New Mexico (Upper Pennsylvanian), its preservational and environmental significance, in: Carboniferous-Permian

512   transition in central New Mexico, edited by: Lucas, S. G., Nelson, W. J., DiMichele, W. A., Speilmann, J. A., Krainer, K.,

513   Barrick, J. E., Elrick, S., and Voigt, S., New Mexico Museum of Natural History and Science, Bulletin, New Mexico Museum

514   of Natural History and Science, Albuquerque, New Mexico, 289–325, 2013.

515   DiMichele, W. A., Bashforth, A. R., Eble, C. F., and Nelson, W. J.: A Middle Pennsylvanian (early Asturian) tropical dry

516   forest, Atokan-Desmoinesian boundary, Illinois Basin, USA, Span. J. Palaeont., 31, 41–84, 2016.

517   Eros, J. M., Montañez, I. P., Osleger, D. A., Davydov, V. I., Nemyrovska, T. I., Poletaev, V. I., and Zhykalyak, M. V.: Sequence

518   stratigraphy and onlap history of the Donets Basin, Ukraine: insight into Carboniferous icehouse dynamics, Palaeogeogr.

519   Palaeocl., 313, 1–25, https://doi.org/10.1016/j.palaeo.2011.08.019, 2012.

520   Falcon-Lang, H. J., Lucas, S. G., Kerp, H., Krainer, K., Montañez, I. P., Vachard, D., Chaney, D. S., Elrick, S. D., Contreras,

521   D. L., Kurzawe, F., DiMichele, W. A., and Looy, C. V.: Early Permian (Asselian) vegetation from a seasonally dry coast in

522   western equatorial Pangea: Paleoecology and evolutionary significance, Palaeogeogr. Palaeocl., 433, 158–173,

523   https://doi.org/10.1016/j.palaeo.2015.05.010, 2015.

524   Falcon-Lang, H. J., Kurzawe, F., and Lucas, S. G.: A Late Pennsylvanian coniferopsid forest in growth position, near Socorro,

525   New Mexico, U.S.A.: tree systematics and palaeoclimatic significance, Rev. Palaeobot. Palyno., 225, 67–83,

526   https://doi.org/10.1016/j.revpalbo.2015.11.008, 2016.

527 Farquhar, G. D., von Caemmerer, S., and Berry, J. A.: A biochemical model of photosynthetic CO_2 assimilation in leaves of

528 C3 species, Planta, 149, 78–90, https://doi.org/10.1007/BF00386231, 1980.

529 Forte, G., Kustatscher, E., van Konijnenburg-van Cittert, J. H. A., Looy, C. V., and Kerp, H.: Conifer diversity in the Kungurian

530 of Europe—Evidence from dwarf-shoot morphology, Rev. Palaeobot. Palyno., 244, 308–315,

531 https://doi.org/10.1016/j.revpalbo.2017.01.004, 2017.

532 Franks, P. J., Royer, D. L., Beerling, D. J., Van de Water, P. K., Cantrill, D. J., Barbour, M. M., and Berry, J. A.: New

533 constraints on atmospheric CO_2 concentration for the Phanerozoic, Geophys. Res. Lett., 41, 4685–4694,

534 https://doi.org/10.1002/2014GL060457, 2014.

535 Gaillardet, J., Dupré, B., Louvat, P., and Allègre, C. J.: Global silicate weathering and CO_2 consumption rates deduced from

536 the chemistry of large rivers, Chem. Geol., 159, 3–30, https://doi.org/10.1016/S0009-2541(99)00031-5, 1999.

537 Gerhart, L. M., and Ward, J. K.: Plant responses to low [CO_2] of the past, New Phytol., 188, 674–695,

538 https://doi.org/10.1111/j.1469-8137.2010.03441.x, 2010.

539 Goddéris, Y., Donnadieu, Y., Carretier, S., Aretz, M., Dera, G., Macouin, M., and Regard, V.: Onset and ending of the late

540 Palaeozoic ice age triggered by tectonically paced rock weathering, Nat. Geosci., 10, 382–386,

541 https://doi.org/10.1038/ngeo2931, 2017.

542 Gradstein, F. M., Ogg, J. G., Schmitz, M., and Ogg, G.: The Geologic Time Scale 2012, Elsevier, 2012.

543 Grossman, E. L., Yancey, T. E., Jones, T. E., Bruckschen, P., Chuvashov, B., Mazzullo, S. J., and Mii, H.-s.: Glaciation,

544 aridification, and carbon sequestration in the Permo-Carboniferous: The isotopic record from low latitudes, Palaeogeogr.

545 Palaeocl., 268, 222–233, https://doi.org/10.1016/j.palaeo.2008.03.053, 2008.

546 Heckel, P. H.: Pennsylvanian stratigraphy of Northern Midcontinent Shelf and biostratigraphic correlation of cyclothems,

547 Stratigraphy, 10, 3–39, 2013.

548 Henderson, C. M.: Permian conodont biostratigraphy, in: The Permian timescale, edited by: Lucas, S. G., and Shen, S.-Z.,

549 Geological Society, London, Special Publications, 1, The Geological Society, London, 119–142, 2018.

550 Hernandez-Castillo, G. R., Rothwell, G. W., and Mapes, G. K.: Thucydiaceae fam. nov., with a review and reevaluation of

551 Paleozoic walchian conifers, Int. J. Plant Sci., 162, 1155–1185, https://doi.org/10.1086/321920, 2001.

29

Hernandez-Castillo, G. R., Rothwell, G. W., Stockey, R. A., and Mapes, G. K.: Growth architecture of *Thucydia mahoningensis*, a model for primitive walchian conifer plants, Int. J. Plant Sci., 164, 443–452, https://doi.org/10.7939/R39S1KW6J, 2003.

Hernandez-Castillo, G. R., Stockey, R. A., Mapes, G. K., and Rothwell, G. W.: A new voltzialean conifer *Emporia royalii* sp. nov. (Emporiaceae) from the Hamilton Quarry, Kansas, Int. J. Plant Sci., 170, 1201–1227, https://doi.org/10.1086/605874, 2009a.

Hernandez-Castillo, G. R., Stockey, R. A., Rothwell, G. W., and Mapes, G. K.: Reconstruction of the Pennsylvanian-age walchian conifer *Emporia cryptica* sp. nov. (Emporiaceae: Voltziales), Rev. Palaeobot. Palyno., 157, 218–237, https://doi.org/10.1016/j.revpalbo.2009.05.003, 2009b.

Hernandez-Castillo, G. R., Stockey, R. A., Rothwell, G. W., and Mapes, G. K.: Reconstructing *Emporia lockardii* (Voltziales: Emporiaceae) and initial thoughts on Paleozoic conifer ecology, Int. J. Plant Sci., 170, 1056–1074, https://doi.org/10.1086/605115, 2009c.

Kerp, H.: The Modernization of Landscapes during the Late Paleozoic-Early Mesozoic, in: Phanerozoic Terrestrial Ecosystems, 2017/07/21 ed., edited by: Gastaldo, R. A., and Dimichele, W. A., The Paleontological Society Papers, Cambridge University Press, Cambridge, U.K., 79–114, 2000.

Kerp, J. H. F., Poort, R. J., Swinkels, H. A. J. M., and Verwer, R.: Aspects of Permian palaeobotany and palynology. IX. conifer-dominated Rotliegend floras from the Saar-Nahe Basin (? Late Carboniferous-early Permian; SW-Germany) with special reference to the reproductive biology of early conifers, Rev. Palaeobot. Palyno., 62, 205–248, https://doi.org/10.1016/0034-6667(90)90090-6, 1990.

Kürschner, W. M., van der Burgh, J., Visscher, H., and Dilcher, D. L.: Oak leaves as biosensors of late Neogene and early Pleistocene paleoatmospheric CO_2 concentrations, Mar. Micropaleontol., 27, 299–312, https://doi.org/10.1016/0377-8398(95)00067-4, 1996.

Looy, C. V.: Extending the range of derived Late Paleozoic conifers: *Lebowskia* gen. nov. (Majonicaceae), Int. J. Plant Sci., 168, 957–972, https://doi.org/10.1086/518256, 2007.

Looy, C. V., and Stevenson, R. A.: Earliest Occurrence of Autorotating Seeds in Conifers: The Permian (Kungurian-Roadian)

577   *Manifera talaris* gen. et sp. nov, Int. J. Plant Sci., 175, 841–854, https://doi.org/10.1086/676973, 2014.

578   Lowry, D. P., Poulsen, C. J., Horton, D. E., Torsvik, T. H., and Pollard, D.: Thresholds for Paleozoic ice sheet initiation,

579   Geology, 42, 627–630, https://doi.org/10.1130/G35615.1, 2014.

580   Lucas, S. G., Allen, B. D., Krainer, K., Barrick, J., Vachard, D., Schneider, J. W., DiMichele, W. A., and Bashforth, A. R.:

581   Precise age and biostratigraphic significance of the Kinney Brick Quarry Lagerstätte, Pennsylvanian of New Mexico, USA,

582   Stratigraphy, 8, 7–27, https://doi.org/10.1086/518256, 2011.

583   Monnin, E., Steig, E. J., Siegenthaler, U., Kawamura, K., Schwander, J., Stauffer, B., Stocker, T. F., Morse, D. C., Barnola, J.

584   M., and Bellier, B.: EPICA Dome C ice core high resolution Holocene and transition CO_2 data, 2004.

585   Montañez, I. P., Tabor, N. J., Niemeier, D., DiMichele, W. A., Frank, T. D., Fielding, C. R., Isbell, J. L., Birgenheier, L. P.,

586   and Rygel, M. C.: CO_2-forced climate and vegetation instability during Late Paleozoic deglaciation, Science, 315, 87–91,

587   https://doi.org/10.1126/science.1134207, 2007.

588   Montañez, I. P.: Modern soil system constraints on reconstructing deep-time atmospheric CO_2, Geochim. Cosmochim. Acta,

589   101, 57–75, https://doi.org/10.1016/j.gca.2012.10.012, 2013.

590   Montañez, I. P., McElwain, J. C., Poulsen, C. J., White, J. D., Dimichele, W. A., Wilson, J. P., Griggs, G., and Hren, M. T.:

591   Climate, $p$$CO_2$ and terrestrial carbon cycle linkages during late Palaeozoic glacial–interglacial cycles, Nat. Geosci., 9, 824–

592   828, https://doi.org/10.1038/ngeo2822, 2016.

593   Myers, D. A., and McKay, E. J.: Geologic map of the north end of the Manzano Mountains, Tijeras and Sedillo quadrangles,

594   Bernalillo County, New Mexico, US Geological Survey, 1976.

595   Myers, T. S., Tabor, N. J., Jacobs, L. L., and Mateus, O.: Estimating soil $p$$CO_2$ using paleosol carbonates: implications for the

596   relationship between primary productivity and faunal richness in ancient terrestrial ecosystems, Paleobiology, 38, 585–604,

597   https://doi.org/10.1666/11005.1, 2012.

598   Myers, T. S., Tabor, N. J., Jacobs, L. L., and Bussert, R.: Effects of Different Organic-Matter Sources On Estimates of

599   Atmospheric and Soil $p$$CO_2$ Using Pedogenic Carbonate, J. Sediment. Res., 86, 800–812, https://doi.org/10.2110/jsr.2016.52,

600   2016.

601   Ogg, J. G., Ogg, G., and Gradstein, F. M.: A concise geologic time scale: 2016, Elsevier, New York, 2016.

Park, J., and Royer, D. L.: Geologic constraints on the glacial amplification of Phanerozoic climate sensitivity, Am. J. Sci., 311, 1–26, https://doi.org/10.2475/01.2011.01, 2011.

Porter, A. S., Yiotis, C., Montañez, I. P., and McElwain, J. C.: Evolutionary differences in $\Delta^{13}C$ detected between spore and seed bearing plants following exposure to a range of atmospheric O_2:CO_2 ratios; implications for paleoatmosphere reconstruction, Geochim. Cosmochim. Acta, 213, 517–533, https://doi.org/10.1016/j.gca.2017.07.007, 2017.

Richey, J. D., Upchurch, G. R., Montañez, I. P., Lomax, B. H., Suarez, M. B., Crout, N. M. J., Joeckel, R. M., Ludvigson, G. A., and Smith, J. J.: Changes in CO_2 during Ocean Anoxic Event 1d indicate similarities to other carbon cycle perturbations, Earth Planet. Sci. Lett., 491, 172–182, https://doi.org/10.1016/j.epsl.2018.03.035, 2018.

Richey, J. D., Montañez, I. P., Goddéris, Y., Looy, C. V., Griffis, N. P., and DiMichele, W. A.: Primary Data from Richey et al., 2020 (Climate Of The Past), https://doi.org/10.25338/B8S90Q, 2020.

Romanek, C. S., Grossman, E. L., and Morse, J. W.: Carbon isotopic fractionation in synthetic aragonite and calcite: Effects of temperature and precipitation rate, Geochim. Cosmochim. Acta, 56, 419–430, https://doi.org/10.1016/0016-7037(92)90142-6, 1992.

Rothwell, G. W., Mapes, G. K., and Mapes, R. H.: Late Paleozoic conifers of North America: structure, diversity and occurrences, Rev. Palaeobot. Palyno., 95, 95–113, https://doi.org/10.1016/S0034-6667(96)00030-9, 1997.

Rothwell, G. W., Mapes, G. K., and Hernandez-Castillo, G. R.: *Hanskerpia* gen. nov. and phylogenetic relationships among the most ancient conifers (Voltziales), Taxon, 54, 733–750, https://doi.org/10.2307/25065430, 2005.

Salley, S., Morales, M., and Sleezer, R. O.: Surficial Geology of the Hamilton Quarry Area, Greenwood County, Kansas, Lawrence, KS, 2005.

Schmitz, M. D., and Davydov, V. I.: Quantitative radiometric and biostratigraphic calibration of the Pennsylvanian–early Permian (Cisuralian) time scale and pan-Euramerican chronostratigraphic correlation, Geol. Soc. Am. Bull., 124, 549–577, https://doi.org/10.1130/B30385.1, 2012.

Šimůnek, Z.: Cuticular analysis of new Westphalian and Stephanian Cordaites species from the USA, Rev. Palaeobot. Palyno., 253, 1–14, https://doi.org/10.1016/j.revpalbo.2018.03.001, 2018.

Stukey, A. H.: Stratigraphic Relations of Pennsylvanian-Permian Strata, Manzanita Mountains, New Mexico, Master's,

627   University of New Mexico, 1967.

628   Tabor, N. J., and Montañez, I. P.: Morphology and distribution of fossil soils in the Permo-Pennsylvanian Wichita and Bowie

629   Groups, north-central Texas, USA: implications for western equatorial Pangean palaeoclimate during icehouse–greenhouse

630   transition, Sedimentology, 51, 851–884, https://doi.org/10.1111/j.1365-3091.2004.00655.x, 2004.

631   Tabor, N. J., and Montañez, I. P.: Oxygen and hydrogen isotope compositions of Permian pedogenic phyllosilicates:

632   development of modern surface domain arrays and implications for paleotemperature reconstructions, Palaeogeogr. Palaeocl.,

633   223, 127–146, https://doi.org/10.1016/j.palaeo.2005.04.009, 2005.

634   Tabor, N. J., DiMichele, W. A., Montañez, I. P., and Chaney, D. S.: Late Paleozoic continental warming of a cold tropical

635   basin and floristic change in western Pangea, Int. J. Coal. Geol., 119, 177–186, https://doi.org/10.1016/j.coal.2013.07.009,

636   2013.

637   Ward, J. K., Harris, J. M., Cerling, T. E., Wiedenhoeft, A., Lott, M. J., Dearing, M.-D., Coltrain, J. B., and Ehleringer, J. R.:

638   Carbon starvation in glacial trees recovered from the La Brea tar pits, southern California, Proc. Natl. Acad. Sci. U.S.A., 102,

639   690–694, https://doi.org/10.1073/pnas.0408315102, 2005.

640   Wardlaw, B. R.: Age assignment of the Pennsylvanian–Early Permian succession of north central Texas, Permophiles, 46, 21–

641   22, 2005.

642   Woodward, F. I.: Stomatal numbers are sensitive to increases in CO_2 from pre-industrial levels, Nature, 327, 617–618,

643   https://doi.org/10.1038/327617a0, 1987.

644   Wynn, J. G.: Carbon isotope fractionation during decomposition of organic matter in soils and paleosols: Implications for

645   paleoecological   interpretations   of   paleosols,   Palaeogeogr.   Palaeocl.,   251,   437–448,

646   https://doi.org/10.1016/j.palaeo.2007.04.009, 2007.

647   Zeebe, R. E., and Caldeira, K.: Close mass balance of long-term carbon fluxes from ice-core CO_2 and ocean chemistry records,

648   Nat. Geosci., 1, 312–315, https://doi.org/10.1038/ngeo185, 2008.